

# Forest response to rising CO<sub>2</sub> drives zonally asymmetric rainfall change over tropical land

Gabriel J. Kooperman<sup>1,2\*</sup>, Yang Chen<sup>1</sup>, Forrest M. Hoffman<sup>3,4</sup>, Charles D. Koven<sup>5</sup>, Keith Lindsay<sup>6</sup>, Michael S. Pritchard<sup>1</sup>, Abigail L. S. Swann<sup>7,8</sup> and James T. Randerson<sup>1</sup>

**Understanding how anthropogenic CO<sub>2</sub> emissions will influence future precipitation is critical for sustainably managing ecosystems, particularly for drought-sensitive tropical forests. Although tropical precipitation change remains uncertain, nearly all models from the Coupled Model Intercomparison Project Phase 5 predict a strengthening zonal precipitation asymmetry by 2100, with relative increases over Asian and African tropical forests and decreases over South American forests. Here we show that the plant physiological response to increasing CO<sub>2</sub> is a primary mechanism responsible for this pattern. Applying a simulation design in the Community Earth System Model in which CO<sub>2</sub> increases are isolated over individual continents, we demonstrate that different circulation, moisture and stability changes arise over each continent due to declines in stomatal conductance and transpiration. The sum of local atmospheric responses over individual continents explains the pan-tropical precipitation asymmetry. Our analysis suggests that South American forests may be more vulnerable to rising CO<sub>2</sub> than Asian or African forests.**

The response of the hydrological cycle to increases in the concentration of atmospheric CO<sub>2</sub> has consequences for global food security and the sustainability of terrestrial ecosystems. In particular, changes in the patterns of precipitation and evapotranspiration may influence the frequency of droughts<sup>1</sup>, forest mortality<sup>2</sup> and freshwater availability<sup>3</sup>. These impacts are especially important in the tropics, where many developing countries are hotspots for climate change vulnerability<sup>4</sup> and where forests are critical for global carbon cycling<sup>5</sup> and biodiversity<sup>6</sup>.

Unfortunately, projections of future precipitation and evapotranspiration from Earth system models (ESMs) participating in the Coupled Model Intercomparison Project Phase 5 (CMIP5)<sup>7</sup> are most uncertain over tropical land<sup>8,9</sup>. Although multi-model mean changes in annual mean precipitation during the twenty-first century driven by the representative concentration pathway 8.5 (RCP8.5) scenario (Fig. 1) can be larger than 1 mm d<sup>-1</sup>, many models predict opposing changes over tropical forests<sup>8</sup>, especially American and African forests where 6 and 10 out of 38 models have responses opposite to the multi-model mean, respectively (Fig. 1, Supplementary Fig. 1 and Supplementary Tables 1 and 2).

## Robust tropical precipitation change

Despite this uncertainty, we have identified a robust pattern of change captured in nearly all high emissions simulations—a growing zonal asymmetry that amplifies precipitation differences between tropical forests in South America and those in Asia and Africa (Fig. 1a–c). Focusing on forests in the Amazon and Indonesian regions (with the latter including Indonesia, Malaysia and Papua New Guinea), this pattern can be quantified using a tropical precipitation asymmetry index ( $I_{TPA}$ ):  $I_{TPA} = P_{\text{Indonesia}} - P_{\text{Amazon}}$ , where  $P$  is annual mean precipitation over forest regions (that is, green areas within purple boxes in Fig. 1f). Present (1986–2005) and future (2081–2100)

precipitation estimates (Fig. 1g) show that, in 36 out of 38 models that were run for the RCP8.5 scenario,  $I_{TPA}$  shifts to more positive values, with a multi-model mean of 1.1 [−0.3, 2.5] mm d<sup>-1</sup> (brackets denote model range; Supplementary Tables 1 and 2).

More broadly across all tropical forests from 23° S to 23° N, including Africa (that is,  $I_{TPA2} = (P_{\text{Asia}} + P_{\text{Africa}}) / 2 - P_{\text{America}}$ , averaged over forest regions within black boxes in Fig. 1f), all RCP8.5 simulations have positive but smaller index increases in asymmetry, with a multi-model mean of 0.7 [0.1, 1.3] mm d<sup>-1</sup> (Supplementary Fig. 1 and Supplementary Table 2). Similarly, in idealized simulations in which CO<sub>2</sub> increases at a rate of 1% yr<sup>-1</sup> from 285 to 1,140 ppm (hereafter referred to as full simulations), all but one model captures a consistent positive trend in  $I_{TPA}$ , with a multi-model mean of 1.5 [−0.6, 2.4] mm d<sup>-1</sup> (Fig. 1h). Eight ESMs were run following the full simulation protocol, with the primary goal of understanding carbon cycle feedbacks<sup>10</sup>. The spatial pattern of precipitation change from the full simulations (Fig. 1c) has a high degree of consistency with the spatial pattern from the same set of models that were run for the RCP8.5 scenario (Fig. 1b), thus highlighting the importance of forcing from atmospheric CO<sub>2</sub> as a primary agent of tropical (and global) precipitation change.

Though CMIP5 models use convective parameterizations that are known to produce biases in the tropics, which can impact soil moisture, evapotranspiration and runoff<sup>8,9,11</sup>, an increase in  $I_{TPA}$  is also seen in a model that avoids parameterization by explicitly simulating deep convection using a kilometre-scale embedded cloud-resolving model (that is, superparameterization<sup>12</sup>, squares in Fig. 1g and Supplementary Fig. 1). Superparameterization improves the representation of organized convection (for example, Madden–Julian Oscillation<sup>12</sup>) and precipitation intensity across the tropics<sup>13</sup>. Consistency between superparameterized and conventional models suggests that the strengthening continental

<sup>1</sup>Department of Earth System Science, University of California, Irvine, Irvine, CA, USA. <sup>2</sup>Department of Geography, University of Georgia, Athens, GA, USA.

<sup>3</sup>Computational Earth Sciences Group and Climate Change Science Institute, Oak Ridge National Laboratory, Oak Ridge, TN, USA. <sup>4</sup>Department of Civil and Environmental Engineering, University of Tennessee, Knoxville, TN, USA. <sup>5</sup>Earth Sciences Division, Lawrence Berkeley National Laboratory, Berkeley, CA, USA. <sup>6</sup>Climate and Global Dynamics Division, National Center for Atmospheric Research, Boulder, CO, USA. <sup>7</sup>Department of Atmospheric Sciences, University of Washington, Seattle, WA, USA. <sup>8</sup>Department of Biology, University of Washington, Seattle, WA, USA. \*e-mail: [kooperman@uga.edu](mailto:kooperman@uga.edu)

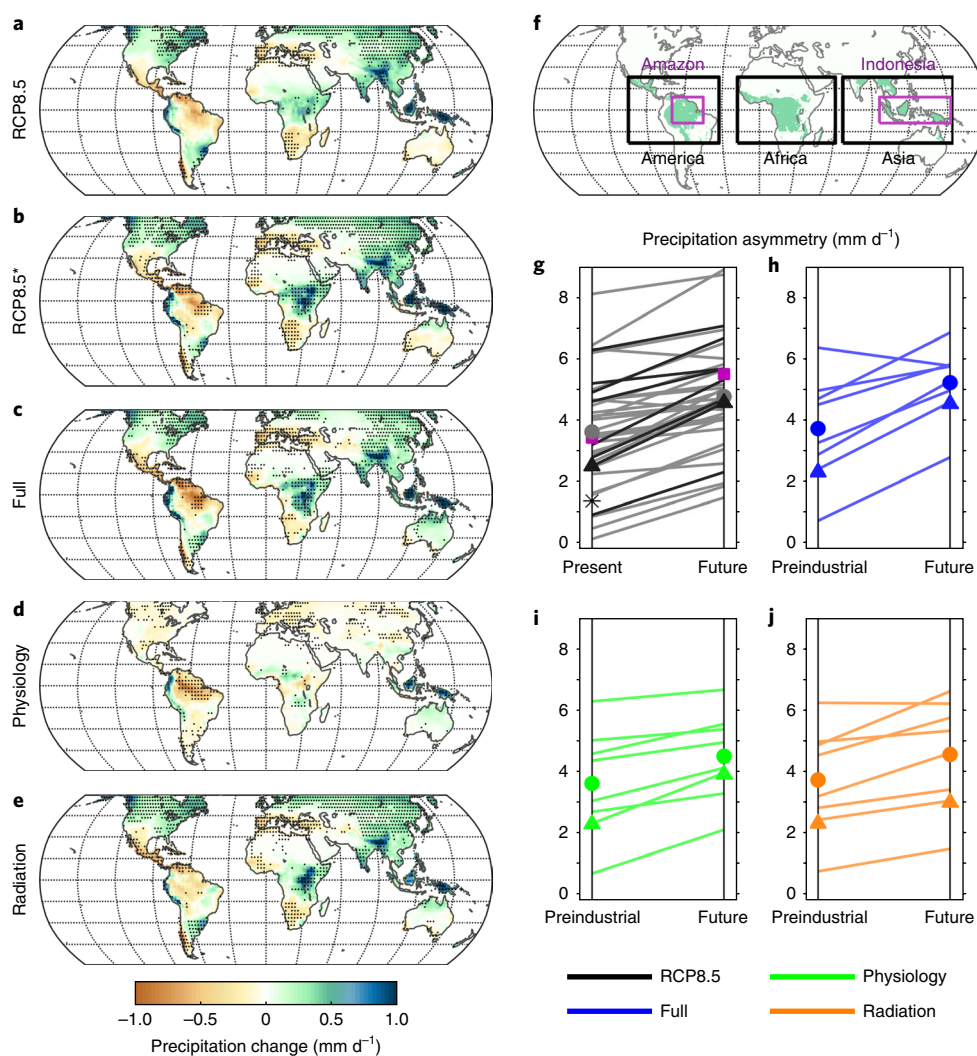


**Fig. 1 | Multi-model mean annual mean precipitation change and tropical precipitation asymmetry index. a–e,** Changes from RCP8.5 (a), RCP8.5\* (subset of eight ESMs used in other simulations; b), full (c), physiology (d) and radiation (e) simulations (the simulations are described in the text and Supplementary Table 4). Stippling indicates where 87.5% of models have the same sign of change (this measure of uncertainty does not account for multiple contributions of different model versions<sup>39</sup>). **f–j,** Tropical forests regions (f) used to calculate the tropical precipitation asymmetry index ( $I_{TPA}$ ; g–j). Symbols in g–j are mean results for all CMIP5 models (circles), CESM (triangles), SPCCSM4 (purple squares) and observations (star). RCP8.5 results are differences between 2081–2100 and 1986–2005, while other simulations are differences between  $4 \times \text{CO}_2$  and preindustrial periods.

asymmetry in precipitation change is robust with respect to the representation of convection.

### Mechanisms of precipitation change

Many studies have investigated mechanisms that drive changes in tropical precipitation, including: changes in the strength of Hadley<sup>14</sup> or Walker circulations<sup>15</sup>, shifts in the intertropical convergence zone<sup>16</sup> or wet-get-wetter responses<sup>17</sup>. These changes involve global or extratropical forcings<sup>14,16</sup>, tropics-wide circulation anomalies<sup>15</sup> and local thermodynamic responses<sup>17,18</sup>. Most global and extratropical mechanisms invoke zonal mean changes in meridional energy transport to explain changes in the strength or position of the Hadley circulation. However, zonal mean changes cannot explain the asymmetric pattern described here for tropical forests across different continents. Several recent studies have attempted to extend the wet-get-wetter scaling mechanism to include horizontal gradients of temperature and humidity<sup>19</sup> or the intertropical convergence zone shift mechanism to include zonal energy fluxes<sup>20</sup>, but neither atmospheric-centric response mechanism fully captures the pattern of change.

Tropics-specific mechanisms, including perturbations to the Walker circulation<sup>15</sup> or patterns of sea surface temperature<sup>18</sup>, which could influence convection and moisture transport<sup>21</sup>, have the potential to create zonally asymmetric responses. However, local changes operating in isolation over individual continents could also modify regional temperature, circulation and moisture transport, enhancing or diminishing precipitation. Local changes over the Amazon may lengthen the dry season due to modulation of orographic dynamics related to the Andes<sup>22,23</sup> or the subtropical jet<sup>24</sup>, while changes over Asia may be associated with the intensity of the Madden–Julian Oscillation<sup>25</sup> or monsoons<sup>26</sup>. In addition, thermodynamic responses associated with regional changes in the horizontal gradients of temperature and humidity can influence local moisture convergence by as much as these dynamical effects<sup>19</sup>.

### Plant physiological response

Plant physiological responses to rising  $\text{CO}_2$  can contribute to precipitation changes by modifying moisture convergence patterns<sup>27</sup>, but it remains to be seen whether these changes are driven by local or remote mechanisms. Here we hypothesize that plant responses

are a primary driver of the growing precipitation asymmetry, by exciting local circulation and thermodynamic changes over individual continents. We tested this hypothesis by regionally isolating the impacts of higher CO<sub>2</sub> in a new set of experiments with the Community Earth System Model (CESM) described below. Atmospheric CO<sub>2</sub> concentration influences the radiative properties of the atmosphere, and the physiological behaviour of terrestrial plants, both of which can drive changes in precipitation<sup>3,27,28</sup>. The direct physiological impact of increasing CO<sub>2</sub> is to increase the CO<sub>2</sub> partial pressure outside leaf stomata. Stomata control gas exchange by adjusting the aperture of their openings in response to CO<sub>2</sub> and other environmental variables, and thus the rate of CO<sub>2</sub> uptake and H<sub>2</sub>O loss (transpiration)<sup>29</sup>. This mechanism connects soil moisture in the vadose zone to the atmosphere and influences the ratio of latent to sensible heating.

As CO<sub>2</sub> increases, stomatal conductance often declines. Without a substantial change in other environmental conditions or leaf area, this decline may reduce the amount of moisture that escapes<sup>30–33</sup> and modify the surface energy budget. In temperate forests, free-air CO<sub>2</sub> enrichment experiments show that canopy-level transpiration declines or remains neutral in mature stands as the concentration of atmospheric CO<sub>2</sub> increases<sup>34</sup>. In tropical forests, carbon isotope and tree-ring growth measurements provide indirect evidence that transpiration has declined over the past 150 years in response to rising CO<sub>2</sub> (ref. <sup>35</sup>). Increases in observed tropical runoff are also consistent with an ecohydrological response to increasing CO<sub>2</sub> (ref. <sup>36</sup>), although changing land use can have first-order impacts in many basins<sup>37</sup>.

### Physiological versus radiative impacts of rising CO<sub>2</sub>

To test the hypothesis that the contribution of reduced stomatal conductance to a growing zonal precipitation asymmetry pattern is robust across different climate models, we analysed carbon cycle simulations from CMIP5. We assessed the relative contribution of radiative and physiological effects on precipitation changes in three sets of simulations that were originally designed to quantify the magnitude of carbon–climate feedbacks<sup>10</sup> (Supplementary Table 4). As described above, eight independent ESMs contributed simulations following this protocol (Supplementary Table 3). In these simulations, atmospheric CO<sub>2</sub> increases from 285 to 1,140 ppm (quadrupling) at a rate of 1% yr<sup>-1</sup>. In one set of simulations, the radiative and physiological effects of CO<sub>2</sub> are simultaneously active (full simulations). In another set, increasing CO<sub>2</sub> solely influences atmospheric radiation, while terrestrial vegetation experiences a constant preindustrial CO<sub>2</sub> concentration (hereafter referred to as radiation simulations). In a third set, increasing CO<sub>2</sub> solely influences terrestrial vegetation, while atmospheric radiation experiences a constant preindustrial CO<sub>2</sub> concentration (hereafter referred to as physiology simulations)<sup>3,10</sup>.

Multi-model mean differences between the first and last 20 years of these simulations show that the pattern of precipitation change in the fully coupled simulations (Fig. 1c) is driven by a combination of physiological (Fig. 1d) and radiative (Fig. 1e) processes. Radiative effects control high-latitude precipitation changes, but tropical changes, particularly over the Amazon, respond more strongly to physiological effects (−0.5 [−0.9, −0.3] versus −0.3 [−0.8, 0.3] mm d<sup>-1</sup>, Supplementary Tables 1 and 3). All models show an increase in  $I_{TPA}$  and  $I_{TPA2}$  when plant physiology responds to rising CO<sub>2</sub> (Fig. 1i) and all but one show an increase in these indices from atmospheric radiative responses (Fig. 1j). Physiology effects yield larger  $I_{TPA}$  increases in half of the models and a slightly larger multi-model mean change (0.9 [0.4, 1.7] mm d<sup>-1</sup>) than radiative effects (0.8 [0, 1.8] mm d<sup>-1</sup>).

### Local versus non-local physiological effects

To determine whether the influence of physiology on the tropical precipitation asymmetry is caused by global, tropics-wide or

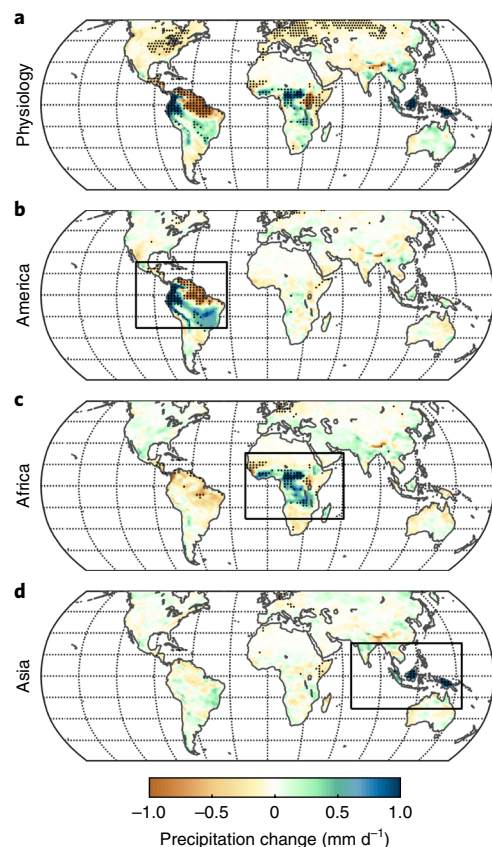


**Fig. 2 | Annual mean precipitation change from the CESM. a–d,** Changes from the CESM (4 × CO<sub>2</sub> minus preindustrial) for physiology (a), America (b), Africa (c) and Asia (d) simulations. All simulations include only the physiological forcing, which is applied regionally in b–d. Stippling in a indicates 90% confidence based on interannual variability, and stippling in b–d indicates where the sign and magnitude of the precipitation change in the regional simulation is at least 50% of statistically significant change in the global physiology simulation.

local-to-continental scale mechanisms, we performed a series of experiments using the CESM version 1 (ref. <sup>38</sup>). In the CESM, physiology contributions to  $I_{TPA}$  are larger than radiative contributions (Supplementary Table 3), and the historical  $I_{TPA}$  value (black triangle in Fig. 1g) falls between the multi-model mean (black circle) and observations (black star). In our new simulations, terrestrial vegetation experiences a CO<sub>2</sub> increase at a rate of 1% yr<sup>-1</sup> up to 1,140 ppm, as in the global physiology simulation, but increases are isolated to the land surface of individual continents, as delineated by the black boxes in Fig. 1f (see Methods for details).

The experiments indicate that local-to-regional scale processes have a first-order control on precipitation changes over each continent, confirming our hypothesis. Changes in mean continental tropical precipitation from the global physiology simulation are mostly captured when CO<sub>2</sub> increases are isolated to individual tropical continents (Fig. 2). Approximately 87% of the increase over Indonesia from the global physiology simulation is produced in the Asia simulation (Supplementary Table 1). Similarly, 59% of the reduction over the Amazon is produced in the America simulation. Changes over South America also include precipitation increases over the Andes, which are captured by the regional physiology forcing. In addition, non-local effects associated with the forcing over Africa further contribute to drying over the Amazon (43%, Supplementary Table 1), which adds almost linearly with local impacts to equal the global physiology response. In addition to exerting non-local controls,

local changes in the Africa simulation have a similar pattern but greater magnitude compared with the global physiology simulation.

Similarities in the patterns of change captured in each region are even more compelling than regional average changes (Fig. 2b–d). The stippling in these panels indicates where the regionally forced simulations capture at least 50% of the global physiology change. Together, the three regionally forced simulations meet these criteria for almost 90% of gridpoints that have a significant precipitation change in the physiology simulation (Fig. 2a) between 23°S and 23°N. Thus, while the magnitude of the local regional change is somewhat lower in the America simulation compared with global physiology (Supplementary Table 1), the pattern is well captured. Focusing on the Amazon and Indonesian regions, where physiological effects are largest, the change in  $I_{TPA}$  is almost a linear combination of the three regionally forced simulations, which contribute 56%, 28% and 12% to the global physiology  $I_{TPA}$  value from the Asia, America and Africa simulations, respectively. The contribution from the Africa simulation to the  $I_{TPA}$  change originates from its influence on winds across the tropical Atlantic Ocean, and thus Amazon rainfall.

### Local thermodynamic and circulation anomalies

Although there is large seasonal and interannual variability in the precipitation signal over Amazon and Indonesian forests, the response to rising  $CO_2$  is consistent across most seasons (except boreal summer in the Amazon and boreal winter in Indonesia) and all phases of the El Niño–Southern Oscillation (Fig. 3). As discussed earlier, higher  $CO_2$  can decrease stomatal conductance and transpiration in mature forest stands, which can reduce total evapotranspiration. This impact is seen clearly in simulated evapotranspiration changes over tropical forests (Fig. 4a–d), which decrease by more than  $0.5 \text{ mm d}^{-1}$ . While the regions defined as forest in these simulations do not change, leaf area can increase from enhanced growth at higher  $CO_2$  levels (Supplementary Fig. 2). However, leaf area is high to begin with in tropical forests, so that  $CO_2$  effects on stomatal conductance have a larger relative influence on canopy conductance, and evapotranspiration still declines. The magnitude of evapotranspiration changes simulated in the global physiology simulation are captured locally in the regionally forced simulations, with only small non-local impacts. In response to decreases in evapotranspiration, the surface energy budget also reaches a new steady state by increasing sensible heat fluxes and surface temperature (Supplementary Fig. 3).

As expected, lower evapotranspiration reduces a local source of moisture to the atmosphere and produces near-surface reductions in specific humidity over each continent (Fig. 4e–h). However, increased convection, collocated in regions of increased precipitation, is associated with local circulation and moisture gradient anomalies that lead to modified patterns of moisture convergence, with upper-level moisture increased over each continent. The surface and upper-level anomalies are horizontally collocated over Indonesian and Central African forests, but over tropical South America, the upper-level humidity increase is displaced over the Andes, while surface and upper-level reductions occur farther east over lowland forests.

Circulation anomalies over South America and Central Africa (Fig. 4) are consistent with a convectively coupled response to enhanced latent heating in the atmosphere by deep convection centred on the Equator, indicating a prominent role of equatorially trapped Kelvin and Rossby waves<sup>39</sup>. This pattern reflects convection in uplift regions to the west (for example, Andes) with weak subsidence to the east (for example, lowland Amazon forests). The local dynamic changes over Asia are weaker, but produce increased low-level convergence from the surrounding waters and greater uplift over the islands (that is, over Sumatra, Java, Borneo and New Guinea).

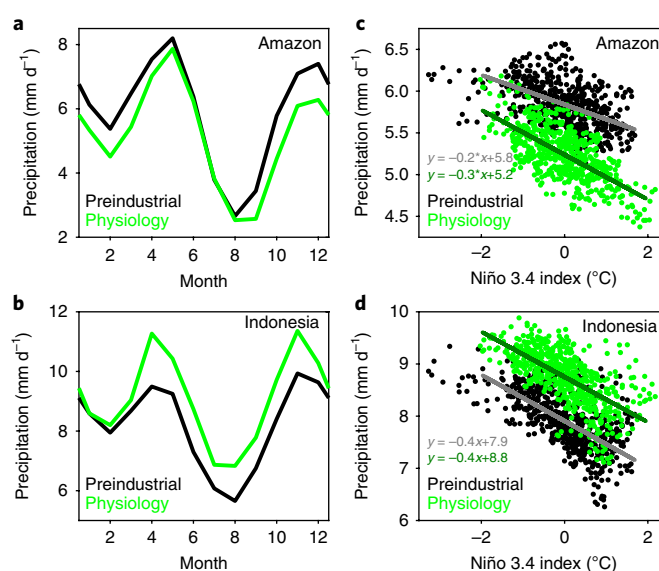


**Fig. 3 | Seasonal and interannual precipitation variability.** a–d, Precipitation seasonal cycle (a,b) and Niño 3.4 index relationship (c,d) over the Amazon (a,c) and Indonesian (b,d) forest regions. Results are from global physiology (green) and preindustrial control (black) simulations. Niño 3.4 index analysis is based on extended simulations for an additional 50 years with fixed preindustrial and  $4 \times CO_2$  concentrations. The Niño 3.4 index is formed from 5-monthly running-mean monthly surface temperature anomalies within the region between 170°–120° W and 5° S–5° N, which is regressed against 12-month running-mean monthly precipitation in the Amazon and Indonesian regions as defined in the text. Regressions are linearly fit for the physiology (dark green) and preindustrial (grey) simulations.

While the response of American and Asian tropical forests to rising  $CO_2$  has little impact on the circulation of other tropical continents, Central African heating exerts some non-local influence. Anomalous eastward flow due to enhanced convective heating over Africa extends far enough across the Atlantic Ocean to counter the mean wind east of South America (Fig. 4c), and contributes to reduced moisture and subsidence over the Amazon (Fig. 4g). This amplifies the present-day influence of circulations associated with the presence of Africa on South America due simply to the proximity of these continents, and the ability of equatorial circulation anomalies, unimpeded by the Coriolis force (that is, large Rossby radius), to act over long distances<sup>40</sup>. This non-local influence contributes to reducing Amazon precipitation in the global physiology and Africa simulations (Fig. 5a and Supplementary Fig. 4).

### Differences between Amazon and Indonesian forests

The response of reduced rainfall over the Amazon to local decreases in stomatal conductance is opposite to that of African and Indonesian forests. The Amazon's greater dependence on local moisture recycling<sup>41</sup>, as well as its interaction with nearby orographic circulations<sup>23</sup>, may make it especially sensitive to  $CO_2$  physiological effects. The reduction from local evapotranspiration limits moisture recycling and accounts for 69% of the Amazon precipitation change in the global physiology simulation (Fig. 5a). The remaining precipitation change is associated with a reduction in moisture convergence due to non-local influences from Africa rather than locally driven changes (Fig. 5a).

Over Indonesia however, there is little non-local influence on either evapotranspiration or moisture convergence, which are driven instead by locally forced changes (Fig. 5b). As expected, lower stomatal conductance reduces local evapotranspiration, but increased

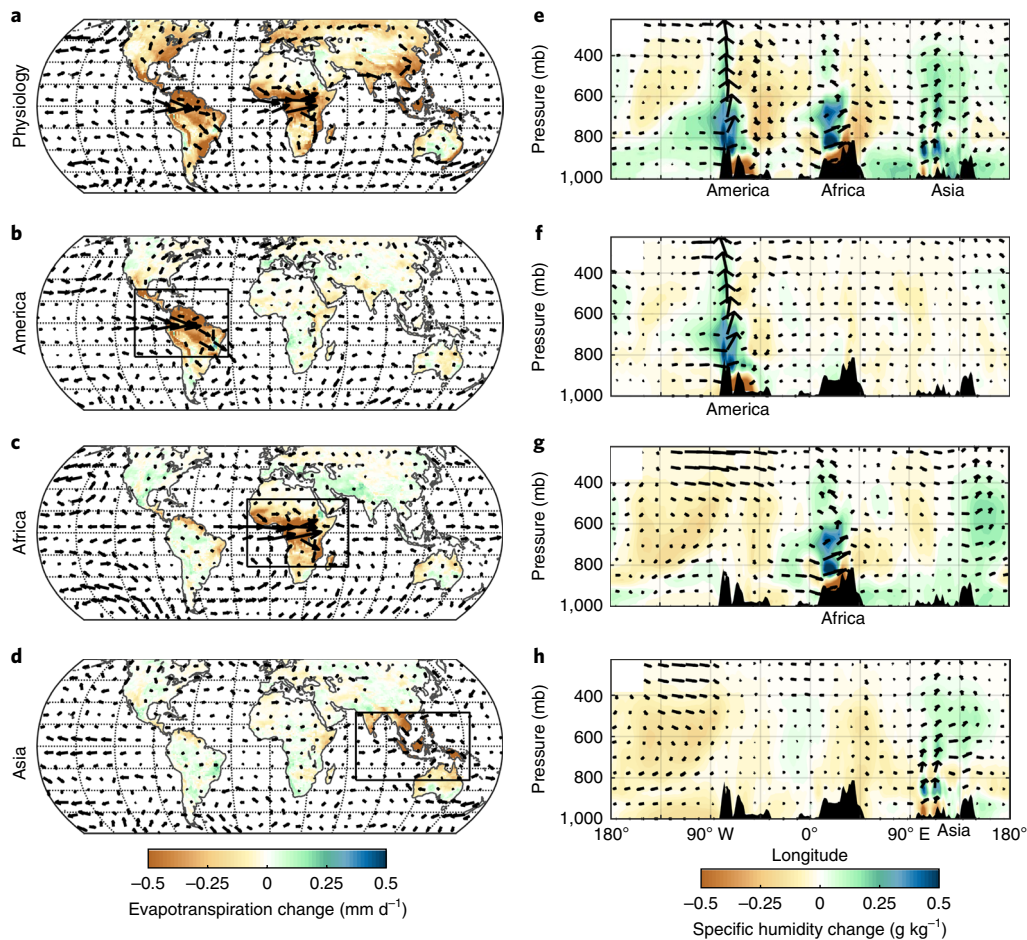


**Fig. 4 | Changes in evapotranspiration and specific humidity. a–h**, Annual mean evapotranspiration (**a–d**) and tropical ( $5^{\circ}\text{S}$ – $5^{\circ}\text{N}$ ) meridional mean specific humidity (**e–h**) change. Changes from the CESM ( $4\times\text{CO}_2$  minus preindustrial) for the physiology (**a,e**), America (**b,f**), Africa (**c,g**) and Asia (**d,h**) simulations. Arrows in **a–d** show the change in 850 mb horizontal wind and arrows in **e–h** show the change in meridional mean zonal and vertical ( $\omega$ ) circulation with pressure as the vertical coordinate.

moisture convergence is larger, leading to higher precipitation over the islands. The different sensitivities of the two regions may result in part from their baseline reliance on local evaporative recycling versus non-local moisture transport as sources of water for precipitation. In simulations and observations, Indonesia receives a much higher fraction of its precipitation from moisture convergence (Supplementary Table 5), which is enhanced in response to  $\text{CO}_2$  forcing.

The decrease in precipitation over the Amazon is also supported by an increase in atmospheric stability (measured by gross moist stability<sup>42,43</sup>) due to an enhanced zonal moist static energy (MSE) gradient (horizontal-thermodynamic component, Fig. 5c) with higher MSE over the mountain slopes to the west and lower to the east of the forest, especially in the 700–900 mb layer (Supplementary Figs. 5–7, see Methods and Supplementary Information for details). In the presence of strong easterlies from regional low-level flow, the enhanced zonal MSE gradient in turn amplifies the efficiency of column MSE export by horizontal advection, leading to overall stabilization and less rainfall over the forest. As a result, more moisture is transported up the slopes of the Andes, which in combination with orographic blocking of anomalous eastward flow from the Pacific, leads to more precipitation over the mountains. This produces a dipole precipitation pattern over the Andes and Amazon that has previously been found in simulations modifying the height of the Andes<sup>23</sup>, simulations of the Last Glacial Maximum and observations of interannual variability<sup>44</sup>. In contrast, increases in precipitation over Indonesia are supported by a decrease in atmospheric stability

resulting from a more bottom-heavy uplift profile in the physiology and Asia simulations (vertical-dynamic component, Fig. 5d), with no contribution from the horizontal components.

## Discussion

Our analysis shows that a robust feature of CMIP5 future projections is a strengthening precipitation asymmetry across tropical continents, with increases in Asian and African forests and decreases in lowland South American forests. Further analysis of idealized  $\text{CO}_2$ -only simulations provides evidence that this pattern is driven by both radiative and physiological responses to rising  $\text{CO}_2$ , which reinforce each other. Over dense tropical forests, physiological effects, which reduce stomatal conductance and lower transpiration, are the largest drivers of precipitation changes<sup>27</sup>. Increasing  $\text{CO}_2$  at the land surface reduces local evapotranspiration by similar magnitudes in all tropical forest regions. Over Indonesia, this reduction is smaller than increases in moisture convergence, so precipitation increases. Over the Amazon the response is more complicated. The forest depends more on local evaporation as its main moisture source, so reductions in evapotranspiration directly impact precipitation. Furthermore, a geographic redistribution of heat and moisture near the altitude of strong regional low-level easterly flow leads to an increase in gross moist stability that is associated with suppressed convection over the forest and greater moisture transport to the Andes. Remote effects from African forests further reduce moisture flow and precipitation over the Amazon.

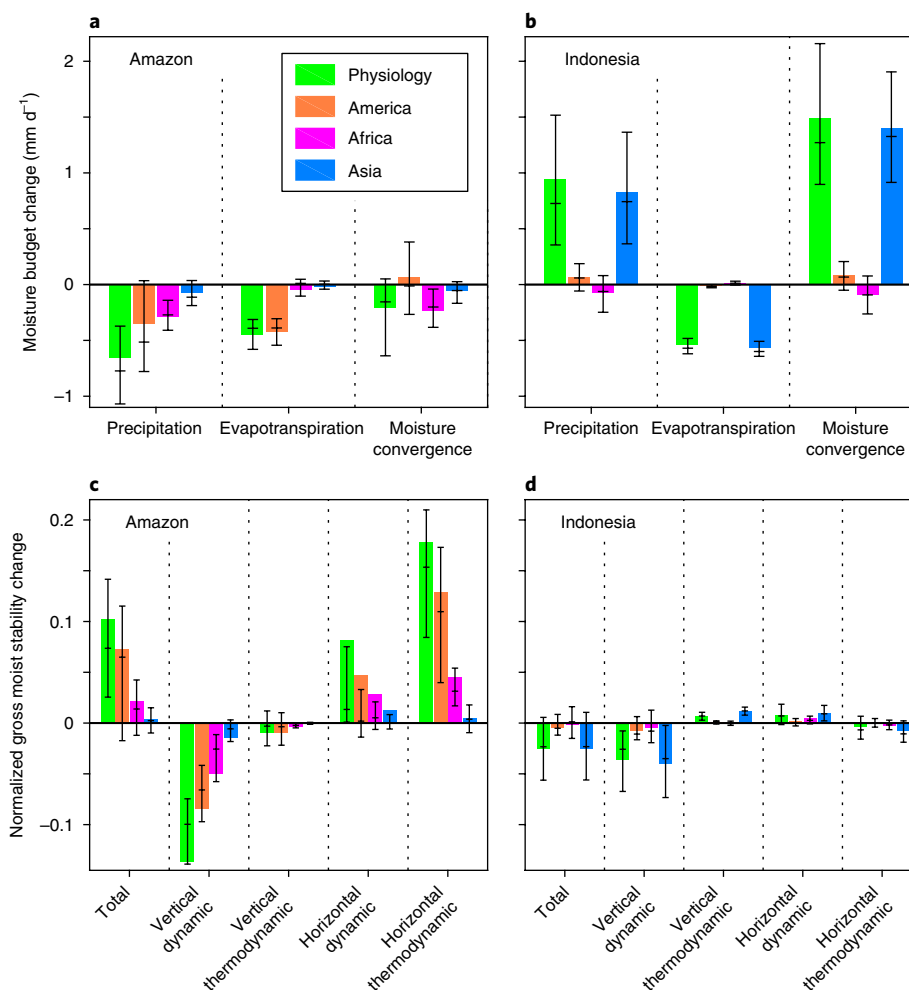


**Fig. 5 | Annual mean moisture budget (precipitation, evapotranspiration and moisture convergence) and normalized gross moist stability changes.** **a–d**, Changes ( $4\times\text{CO}_2$  minus preindustrial) are averaged over the Amazon (**a,c**) and Indonesian (**b,d**) forest regions (purple boxes in Fig. 1f) from the CESM for the physiology, America, Africa and Asia simulations. The normalized gross moist stability changes in **c** and **d** are further decomposed into vertical-dynamic, vertical-thermodynamic, horizontal-dynamic and horizontal-thermodynamic components as described in the Methods. Solid lines indicate the interquartile range (25th, 50th and 75th percentile values) based on the spatial variability from gridpoints used in the regional average.

This analysis highlights the need to improve our understanding of the physiological response of tropical trees to rising  $\text{CO}_2$ . New free-air  $\text{CO}_2$  enrichment experiment measurements from the tropics will be essential for reducing uncertainties in the representation of stomatal conductance and photosynthesis coupling mechanisms in ESMs. As the majority of precipitation change above tropical forests is captured by the atmospheric response to local physiological forcing, regional high-resolution models that resolve orography and more complex ecosystem processes may be useful tools in future work to better understand the role of land–surface interactions in shaping projections of precipitation change. While previous work has identified the Amazon as a region of high vulnerability for future climate change, our analysis demonstrates that this regional response is completely different from other tropical forests, which are more likely to experience decreasing moisture stress. Radiative and physiological responses to rising  $\text{CO}_2$  may be further amplified by land-use change and deforestation, which have also been shown to reduce precipitation over the Amazon<sup>45</sup>, increasing the prevalence of drought<sup>1</sup> and putting the region at greater risk for forest fires<sup>24</sup>. All tropical forests are threatened biodiversity hotspots, but the Amazon has more terrestrial plant and vertebrate species than any other region<sup>6</sup>, and thus plant physiological responses to rising  $\text{CO}_2$  present a threat to biodiversity loss on a global scale.

Furthermore, the Amazon's dominant role as a terrestrial carbon sink implies that its future health may have critical consequences for the growth rate of atmospheric  $\text{CO}_2$  and global climate<sup>5</sup>.

## Methods

Methods, including statements of data availability and any associated accession codes and references, are available at <https://doi.org/10.1038/s41558-018-0144-7>.

Received: 13 July 2017; Accepted: 27 March 2018;  
Published online: 27 April 2018

## References

- Allen, C. D. et al. A global overview of drought and heat-induced tree mortality reveals emerging climate change risks for forests. *For. Ecol. Manag.* **259**, 660–684 (2010).
- Phillips, O. L. et al. Drought–mortality relationships for tropical forests. *New Phytol.* **187**, 631–646 (2010).
- Swann, A. L. S., Hoffman, F. M., Koven, C. D. & Randerson, J. T. Plant responses to increasing  $\text{CO}_2$  reduce estimates of climate impacts on drought severity. *Proc. Natl Acad. Sci. USA* **113**, 10019–10024 (2016).
- Diffenbaugh, N. S. & Giorgi, F. Climate change hotspots in the CMIP5 global climate model ensemble. *Climatic Change* **114**, 813–822 (2012).
- Cox, P. et al. Amazonian forest die back under climate–carbon cycle projections for the 21st century. *Theor. Appl. Climatol.* **78**, 137–156 (2004).

6. Mittermeier, R. A. et al. Wilderness and biodiversity conservation. *Proc. Natl Acad. Sci. USA* **100**, 10309–10313 (2003).
7. Taylor, K. E., Stouffer, R. J. & Meehl, G. A. An overview of CMIP5 and the experiment design. *Bull. Am. Meteorol. Soc.* **93**, 485–498 (2012).
8. IPCC *Climate Change 2013: The Physical Science Basis* (eds Stocker, T. F. et al.) (Cambridge Univ. Press, 2013).
9. Yin, L., Fu, R., Shevliakova, E. & Dickinson, R. E. How well can CMIP5 simulate precipitation and its controlling processes over tropical South America? *Clim. Dynam.* **41**, 3127–3143 (2013).
10. Arora, V. K. et al. Carbon–concentration and carbon–climate feedbacks in CMIP5 Earth system models. *J. Clim.* **26**, 5289–5314 (2013).
11. Sun, Y., Solomon, S., Dai, A. & Portmann, R. W. How often does it rain? *J. Clim.* **19**, 916–934 (2006).
12. Randall, D., Khairoutdinov, M., Arakawa, A. & Grabowski, W. Breaking the cloud parameterization deadlock. *Bull. Am. Meteorol. Soc.* **84**, 1547–1564 (2003).
13. Kooperman, G. J., Pritchard, M. S., Burt, M. A., Branson, M. D. & Randall, D. A. Robust effects of cloud superparameterization on simulated daily rainfall intensity statistics across multiple versions of the Community Earth System Model. *J. Adv. Model. Earth Syst.* **8**, 1–26 (2016).
14. Swann, A. L. S., Fung, I. Y. & Chiang, J. C. H. Mid-latitude afforestation shifts general circulation and tropical precipitation. *Proc. Natl Acad. Sci. USA* **109**, 712–716 (2012).
15. Vecchi, G. A. & Harrison, M. J. Weakening of tropical Pacific atmospheric circulation due to anthropogenic forcing. *Nature* **441**, 73–76 (2006).
16. Kang, S. M., Held, I. M., Frierson, D. M. W. & Zhao, M. The response of the ITCZ to extratropical thermal forcing: idealized slab-ocean experiments with a GCM. *J. Clim.* **21**, 3521–3532 (2008).
17. Held, I. M. & Soden, B. J. Robust responses of the hydrological cycle to global warming. *J. Clim.* **19**, 5686–5699 (2006).
18. Xie, S.-P. et al. Global warming pattern formation: sea surface temperature and rainfall. *J. Clim.* **23**, 966–986 (2010).
19. Byrne, M. P. & O’Gorman, P. A. The response of precipitation minus evapotranspiration to climate warming: why the “wet-get-wetter, dry-get-drier” scaling does not hold over land. *J. Clim.* **28**, 8078–8092 (2015).
20. Boos, W. R. & Korty, R. L. Regional energy budget control of the intertropical convergence zone and application to mid-Holocene rainfall. *Nat. Geosci.* **9**, 892–897 (2016).
21. van der Ent, R. J. & Savenije, H. H. G. Oceanic sources of continental precipitation and the correlation with sea surface temperature. *Water Resour. Res.* **49**, 3993–4004 (2013).
22. Cook, K. H. & Vizy, E. K. Effects of twenty-first-century climate change on the Amazon rainforest. *J. Clim.* **21**, 542–560 (2008).
23. Insel, N., Poulsen, C. J. & Ehlers, T. A. Influence of the Andes Mountains on South American moisture transport, convection, and precipitation. *Clim. Dynam.* **35**, 1477–1492 (2010).
24. Fu, R. et al. Increased dry-season length over southern Amazonia in recent decades and its implication for future climate projection. *Proc. Natl Acad. Sci. USA* **110**, 18110–18115 (2013).
25. Arnold, N. P., Branson, M., Kuang, Z., Randall, D. & Tziperman, E. MJO intensification with warming in the superparameterized CESM. *J. Clim.* **28**, 2706–2724 (2015).
26. Turner, A. G. & Annamalai, H. Climate change and the South Asian summer monsoon. *Nat. Clim. Change* **2**, 587–595 (2012).
27. Pu, B. & Dickinson, R. E. Hydrological changes in the climate system from leaf responses to increasing CO<sub>2</sub>. *Clim. Dynam.* **42**, 1905–1923 (2014).
28. Sellers, P. J. et al. Comparison of radiative and physiological effects of doubled atmospheric CO<sub>2</sub> on climate. *Science* **271**, 1402–1406 (1996).
29. Cowan, I. R. Stomatal behaviour and environment. *Adv. Bot. Res.* **4**, 117–228 (1977).
30. Field, C. B., Jackson, R. B. & Mooney, H. A. Stomatal responses to increased CO<sub>2</sub>: implications from the plant to the global scale. *Plant Cell Environ.* **18**, 1214–1225 (1995).
31. Ball, J. T., Woodrow, I. E. & Berry, J. A. in *Progress in Photosynthesis Research* (ed. Biggins, J.) 221–224 (Springer, Dordrecht, 1987).
32. Medlyn, B. E. et al. Stomatal conductance of forest species after long-term exposure to elevated CO<sub>2</sub> concentration: a synthesis. *New Phytol.* **149**, 247–264 (2001).
33. Medlyn, B. E. et al. Reconciling the optimal and empirical approaches to modeling stomatal conductance. *Glob. Change Biol.* **17**, 2134–2144 (2011).
34. De Kauwe, M. G. et al. Forest water use and water use efficiency at elevated CO<sub>2</sub>: a model-data intercomparison at two contrasting temperate forest FACE sites. *Glob. Change Biol.* **19**, 1759–1779 (2013).
35. van der Sleen, P. et al. No growth stimulation of tropical trees by 150 years of CO<sub>2</sub> fertilization but water-use efficiency increased. *Nat. Geosci.* **8**, 24–28 (2015).
36. Gedney, N. et al. Detection of a direct carbon dioxide effect in continental river runoff records. *Nature* **439**, 835–838 (2006).
37. Coe, M. T., Costa, M. H. & Soares-Filho, B. S. The influence of historical and potential future deforestation on the stream flow of the Amazon River–land surface processes and atmospheric feedbacks. *J. Hydrol.* **369**, 165–174 (2009).
38. Lindsay, K. et al. Pre-industrial-control and twentieth-century carbon cycle experiments with the Earth system model CESM1(BGC). *J. Clim.* **27**, 8981–9005 (2014).
39. Gill, A. E. Some simple solutions for heat-induced tropical circulation. *Q. J. R. Meteorol. Soc.* **106**, 447–462 (1980).
40. Cook, K. H., Hsieh, J.-S. & Hagos, S. M. The Africa–South America intercontinental teleconnection. *J. Clim.* **17**, 2851–2865 (2004).
41. Spracklen, D. V., Arnold, S. R. & Taylor, C. M. Observations of increased tropical rainfall preceded by air passage over forests. *Nature* **489**, 282–285 (2012).
42. Inoue, K. & Back, L. Column-integrated moist static energy budget analysis on various time scales during TOGA COARE. *J. Atmos. Sci.* **72**, 1856–1871 (2015).
43. Raymond, D. J., Sessions, S. L., Sobel, A. H. & Fuchs, Z. The mechanics of gross moist stability. *J. Adv. Model. Earth Syst.* **1**, 1–20 (2009).
44. Vizy, E. K. & Cook, K. H. Relationship between Amazon and high Andes rainfall. *J. Geophys. Res.* **112**, 1–14 (2007).
45. Malhi, Y. et al. Exploring the likelihood and mechanism of a climate-change-induced die back of the Amazon rainforest. *Proc. Natl Acad. Sci. USA* **106**, 20610–20615 (2009).
48. Lintner, B. R. et al. Characterizing CMIP5 model spread in simulated rainfall in the Pacific Intertropical Convergence and South Pacific Convergence zones. *J. Geophys. Res. Atmos.* **121**, 590–607 (2016).

## Acknowledgements

G.J.K., Y.C. and J.T.R. acknowledge support from the Gordon and Betty Moore Foundation (GBMF3269). C.D.K., F.M.H., M.S.P. and J.T.R. acknowledge support from the US Department of Energy (DOE) Office of Science Biological and Environmental Research programmes. The DOE support includes funding from the Regional and Global Climate Modeling programme to the Reducing Uncertainties in Biogeochemical Interactions through Synthesis and Computation (RUBISCO) Scientific Focus Area, from the Terrestrial Ecosystem Sciences programme to the Next Generation Ecosystem Experiments — Tropics, and from the Early Career programme (DE-SC0012152). K.L. acknowledges support from the National Center for Atmospheric Research (NCAR), which is sponsored by the US National Science Foundation (NSF). A.L.S.S. acknowledges support from the NSF (AGS-1321745 and AGS-1553715). CESM development is led by NCAR and supported by the NSF and DOE. CESM simulations were run at the NSF NCAR Computational and Information Systems Laboratory on Yellowstone (P36271028).

## Author contributions

All authors contributed to designing the experiment, interpreting the results and editing the manuscript. G.J.K. performed the simulations, carried out the analysis and drafted the manuscript. M.S.P. conducted the moist stability analysis.

## Competing interests

The authors declare no competing interests.

## Additional information

**Supplementary information** is available for this paper at <https://doi.org/10.1038/s41558-018-0144-7>.

**Reprints and permissions information** is available at [www.nature.com/reprints](http://www.nature.com/reprints).

**Correspondence and requests for materials** should be addressed to G.J.K.

**Publisher’s note:** Springer Nature remains neutral with regard to jurisdictional claims in published maps and institutional affiliations.

## Methods

**Experimental design.** This study investigates precipitation changes in three sets of simulations. Evaluation of CMIP5 RCP8.5 simulations demonstrates that a zonally asymmetric tropical precipitation change pattern is ubiquitous in global climate model simulations of the twenty-first century under a business-as-usual emissions scenario. Evaluation of idealized CMIP5 ESM simulations demonstrates that the physiological response of plants is the primary driver of this pattern over dense tropical forest regions. Evaluation of CESM simulations in which the CO<sub>2</sub> physiological forcing is applied over individual tropical continents demonstrates that locally driven changes in evapotranspiration and moisture convergence capture the majority of the pan-tropical precipitation change, with a small non-local contribution of reduced precipitation over the Amazon associated with the forcing over Central Africa. Each set of simulations, as well as the observations used for comparison, are described in detail below.

**CMIP5 RCP8.5 simulations.** This study evaluated output from 38 models (references for each model are given in Supplementary Table 2, refs <sup>46–81</sup>) contributing historical and RCP8.5 simulations to CMIP5<sup>7</sup>. Both simulation sets use fully coupled model configurations with interactive atmosphere, land, ocean and sea-ice components. Boundary conditions for the historical simulations included the observed time series of greenhouse gas concentrations and best-estimate time series of aerosol particle emissions. The RCP8.5 simulations were performed with increasing greenhouse gases and aerosol particle emissions from 2006 to 2100 (reaching approximately 1,370 ppm CO<sub>2</sub>-equivalent mole fraction by 2100 (ref. <sup>82</sup>)). Averages from 1986–2005 and 2081–2100 provide climatological conditions for present and future periods, respectively (Supplementary Table 4).

**CMIP5 ESM simulations.** This study also evaluated output from a CMIP5 experiment designed to assess carbon–climate feedbacks<sup>10</sup>. Eight models (references for each model are given in Supplementary Table 3) participated in this experiment in which the concentration of CO<sub>2</sub> increased at a rate of 1% yr<sup>-1</sup> from 285 (preindustrial) to 1,140 ppm (4×CO<sub>2</sub>) for radiation and biogeochemistry (full, 1pctCO2), radiation only (radiation, esmFdbk1) and biogeochemistry only (physiology, esmFixClim1). In the radiation and physiology simulations, CO<sub>2</sub> was held at preindustrial levels (285 ppm) for biogeochemistry and radiation submodels, respectively. Averages of the first and last 20 years provide preindustrial and future conditions, respectively (Supplementary Table 4).

**CESM simulations.** We performed an additional set of new simulations using CESM1.0.6(BGC), applying the biogeochemistry-only CO<sub>2</sub> forcing to land surfaces globally (physiology) and isolated over tropical (23°S–23°N) America, Africa and Asia (black boxes in Fig. 1f). The CESM is a fully coupled ESM with active biogeochemistry<sup>18</sup>, and the Community Atmosphere Model<sup>83</sup> and Community Land Model<sup>84</sup> as atmospheric and land components, respectively. In the CESM, the representation of stomata conductance is based on the Ball–Berry model and is given as the inverse of leaf stomatal resistance:  $\frac{1}{r_s} = m \frac{A_{cs}}{c_s e_s} p_{\text{atm}} + b$ , where  $r_s$  is leaf stomatal resistance,  $m$  is a plant-functional-type-dependent parameter,  $A$  is leaf photosynthesis,  $c_s$  is the CO<sub>2</sub> partial pressure at the leaf surface,  $e_s$  is the vapour pressure at the leaf surface,  $e_s$  is the saturation vapour pressure inside the leaf,  $p_{\text{atm}}$  is the atmospheric pressure and  $b$  is the minimum conductance. For CESM simulations, an average of the 20 years before increasing CO<sub>2</sub> provides preindustrial conditions that are consistent for all cases. Averages of the last 20 years of each case provide future conditions (Supplementary Table 4).

**SPCCSM4 simulation.** Results from the Superparameterized Community Climate System Model version 4 (SPCCSM4) RCP8.5 simulation are also included in Fig. 1, Supplementary Fig. 1 (squares) and Supplementary Table 2, but are not used in the multi-model mean calculation (that is, Supplementary Table 1). The superparameterization approach applies simplified cloud-resolving models to represent unresolved subgrid moist convection explicitly rather than using conventional convective parameterizations<sup>12</sup>. In the SPCCSM4 simulation analysed here, each column of the Community Atmosphere Model contains an independent (that is, periodic boundary conditions), two-dimensional, cloud-resolving model configured with 32 columns at 3 km resolution oriented in the east–west direction<sup>81</sup>.

**Observations.** We used observed present-day (2002 to 2011) precipitation and evapotranspiration data from the Global Precipitation Climatology Project One-Degree Daily product (GPCP<sup>85</sup>) and Global Land Evaporation Amsterdam Model product (GLEAM<sup>86</sup>), respectively.

**Regional analysis.** For the calculation of  $I_{\text{TPA}}$  and  $I_{\text{TPA}^{\Delta}}$ , the model output and observational data were interpolated to 0.25° resolution and a consistent tropical forest and woodland mask (shown as the green areas in Fig. 1f) was used for an area-weighted calculation of annual mean precipitation in each region.

**Gross moist stability analysis.** Gross moist stability was normalized (NGMS) using a simplified formulation following equation (3) in ref. <sup>42</sup>, with constituent variables estimated numerically using annual mean fields pre-interpolated

vertically onto a high-resolution (5 hPa) pressure grid, and with centred finite differences to estimate vertical and horizontal (spherical) gradients of temperature ( $T$ ), water vapour ( $Q$ ) and geopotential height ( $Z$ ). Following ref. <sup>87</sup>, a  $7^\circ \times 7^\circ$  horizontal smoother was applied. NGMS was decomposed into horizontal and vertical components following equation (4) in ref. <sup>42</sup>. This decomposition separates the changes in horizontal winds ( $U$  and  $V$ ) and moist static energy gradients (that is, horizontal component) from the changes in vertical winds (omega) and moist static energy gradients (that is, vertical component). To determine the degree to which changes in circulation (that is, dynamics) versus changes in the vertical profiles and horizontal gradients of heat and water vapour (that is, thermodynamics) control the total NGMS change, we further decompose the horizontal and vertical components into dynamic and thermodynamic components. This decomposition is achieved by calculating NGMS using the preindustrial circulation from the control simulation (that is,  $U$ ,  $V$  and omega) with physiological thermodynamics (that is,  $Q$ ,  $T$  and  $Z$ ) for the thermodynamic component and vice versa for the dynamic component. Results of the decomposition are presented in Fig. 5c,d, and further discussion of this analysis is provided in the Supplementary Information.

**Data availability.** CMIP5 RCP8.5 and ESM output (precipitation variable: pr) is available on the Earth System Grid (<http://esgf.llnl.gov>). CESM output is available from the corresponding author and archived at the National Center for Atmospheric Research. GPCP data are available from <http://precip.gsfc.nasa.gov> and GLEAM data are available from <http://www.gleam.eu>.

## References

- Bi, D. et al. The ACCESS coupled model: description, control climate and evaluation. *Aust. Meteorol. Oceanogr. J.* **63**, 41–64 (2013).
- Dix, M. et al. The ACCESS coupled model: documentation of core CMIP5 simulations and initial results. *Aust. Meteorol. Oceanogr. J.* **63**, 83–99 (2013).
- Gent, P. R. et al. The Community Climate System Model Version 4. *J. Clim.* **24**, 4973–4991 (2011).
- Long, M. C., Lindsay, K., Peacock, S., Moore, J. K. & Doney, S. C. Twentieth-century oceanic carbon uptake and storage in CESM1(BGC). *J. Clim.* **26**, 6775–6800 (2012).
- Hurrell, J. et al. The Community Earth System Model: a framework for collaborative research. *Bull. Am. Meteorol. Soc.* **94**, 1339–1360 (2013).
- Fogli, P. G. et al. *INGV-CMCC Carbon (ICC): A Carbon Cycle Earth System Model* (Euro-Mediterranean Center on Climate Change, 2009).
- Vichi, M. et al. Global and regional ocean carbon uptake and climate change: sensitivity to a substantial mitigation scenario. *Clim. Dynam.* **37**, 1929–1947 (2011).
- Soccimarro, E. et al. Effects of tropical cyclones on ocean heat transport in a high resolution coupled general circulation model. *J. Clim.* **24**, 4368–4384 (2011).
- Voldoire, A. et al. The CNRM-CM5.1 global climate model: description and basic evaluation. *Clim. Dynam.* **40**, 2091–2121 (2013).
- Rotstayn, L. D. et al. Aerosol- and greenhouse gas-induced changes in summer rainfall and circulation in the Australasian region: a study using single-forcing climate simulations. *Atmos. Chem. Phys.* **12**, 6377–6404 (2012).
- Arora, V. K. et al. Carbon emission limits required to satisfy future representative concentration pathways of greenhouse gases. *Geophys. Res. Lett.* **38**, L05805 (2011).
- von Salzen, K. et al. The Canadian Fourth Generation Atmospheric Global Climate Model (CanAM4). Part I: representation of physical processes. *Atmos. Ocean* **51**, 104–125 (2013).
- Hazeleger, W. et al. EC-Earth V2.2: description and validation of a new seamless Earth system prediction model. *Clim. Dynam.* **39**, 2611–2629 (2012).
- Qiao, F. et al. Development and evaluation of an Earth system model with surface gravity waves. *J. Geophys. Res. Oceans* **118**, 4514–4524 (2013).
- Delworth, T. L. et al. GFDL's CM2 global coupled climate models. Part I: formulation and simulation characteristics. *J. Clim.* **19**, 643–674 (2006).
- Donner, L. J. et al. The dynamical core, physical parameterizations, and basic simulation characteristics of the atmospheric component AM3 of the GFDL global coupled model CM3. *J. Clim.* **24**, 3484–3519 (2011).
- Dunne, J. P. et al. GFDL's ESM2 global coupled climate–carbon Earth system models. Part I: physical formulation and baseline simulation characteristics. *J. Clim.* **25**, 6646–6665 (2012).
- Dunne, J. P. et al. GFDL's ESM2 global coupled climate–carbon Earth system models Part II: carbon system formulation and baseline simulation characteristics. *J. Clim.* **26**, 2247–2267 (2013).
- Schmidt, G. A. et al. Present day atmospheric simulations using GISS Model: comparison to in-situ, satellite and reanalysis data. *J. Clim.* **19**, 153–192 (2006).
- Collins, W. J. et al. Development and evaluation of an Earth-system model HadGEM2. *Geosci. Model Dev.* **4**, 1051–1075 (2011).
- Martin, G. M. et al. The HadGEM2 family of Met Office unified model climate configurations. *Geophys. Model Dev.* **4**, 723–757 (2011).

67. Jones, C. D. et al. The HadGEM2-ES implementation of CMIP5 centennial simulations. *Geosci. Model Dev.* **4**, 543–570 (2011).
68. Dufresne, J.-L. et al. Climate Change projections using the IPSL-CM5 Earth system model: from CMIP3 to CMIP5. *Clim. Dynam.* **40**, 2123–2165 (2013).
69. Watanabe, M., Chikira, M., Imada, Y. & Kimoto, M. Convective control of ENSO simulated in MIROC. *J. Clim.* **24**, 543–562 (2011).
70. Watanabe, M. et al. Improved climate simulation by MIROC5: mean states, variability, and climate sensitivity. *J. Clim.* **23**, 6312–6335 (2010).
71. Giorgetta, M. A. et al. Climate and carbon cycle changes from 1850 to 2100 in MPI-ESM simulations for the Coupled Model Intercomparison Project Phase 5. *J. Adv. Model. Earth Syst.* **5**, 572–597 (2013).
72. Yukimoto, S. et al. *Meteorological Research Institute-Earth System Model v1 (MRI-ESM1) Model Description* (MRI, 2011).
73. Yukimoto, S. et al. A new global climate model of the Meteorological Research Institute: MRI-CGCM3—model description and basic performance. *J. Meteorol. Soc. Jpn.* **90A**, 23–64 (2012).
74. Adachi, Y. et al. Basic performance of a new Earth system model of the Meteorological Research Institute (MRI-ESM1). *Pap. Meteorol. Geophys.* **64**, 1–19 (2013).
75. Tjiputra, J. F. et al. Evaluation of the carbon cycle components in the Norwegian Earth System Model (NorESM). *Geophys. Model Dev.* **6**, 301–325 (2013).
76. Iversen, T. et al. The Norwegian Earth System Model, NorESM1–M. Part 2: climate response and scenario projections. *Geosci. Model Dev.* **6**, 1–27 (2013).
77. Wu, T. A mass-flux cumulus parameterization scheme for large-scale models: description and test with observations. *Clim. Dynam.* **38**, 725–744 (2012).
78. Xin, X. et al. How well does BCC\_CSM1.1 reproduce the 20th century climate change over China? *Atmos. Ocean Sci. Lett.* **6**, 21–26 (2012).
79. Xin, X., Zhang, L., Zhang, J., Wu, T. & Fang, Y. Climate change projections over East Asia with BCC\_CSM1.1 climate model under RCP scenarios. *J. Meteorol. Soc. Jpn.* **91**, 413–429 (2013).
80. Volodin, E. M., Dianskii, N. A. & Gusev, A. V. Simulating present-day climate with the INMCM4.0 coupled model of the atmospheric and oceanic general circulations. *Izv. Atmos. Ocean Phys.* **46**, 414–431 (2010).
81. Stan, C. & Xu, L. Climate simulations and projections with a superparameterized climate model. *Environ. Model. Softw.* **60**, 134–152 (2014).
82. Moss, R. H. et al. The next generation of scenarios for climate change research and assessment. *Nature* **463**, 747–756 (2010).
83. Neale, R. B. et al. *NCAR Technical Note: Description of the NCAR Community Atmosphere Model (CAM 4.0)* (National Center for Atmospheric Research, 2010).
84. Lawrence, D. M. et al. Parameterization improvements and functional and structural advances in version 4 of the Community Land Model. *J. Adv. Model. Earth Syst.* **3**, 1–27 (2011).
85. Huffman, G. J. et al. Global precipitation at one-degree daily resolution from multi-satellite observations. *J. Hydrometeorol.* **2**, 36–50 (2001).
86. Miralles, D. G. et al. Global land-surface evaporation estimated from satellite-based observations. *Hydrol. Earth Syst. Sci.* **15**, 453–469 (2011).
87. Benedict, J. J., Maloney, E. D., Sobel, A. H. & Frierson, D. M. Gross moist stability and MJO simulation skill in three full-physics GCMs. *J. Atmos. Sci.* **71**, 3327–3349 (2014).